

# First hard X-ray observations of the blazar S5 0716+714 with *NuSTAR* during a multiwavelength campaign

A. Wierzcholska<sup>1</sup> and H. Siejkowski<sup>2</sup>†,

<sup>1</sup>*Institute of Nuclear Physics, Polish Academy of Sciences, ul. Radzikowskiego 152, PL-31-342 Kraków, Poland*

<sup>2</sup>*AGH University of Science and Technology, ACC Cyfronet AGH, ul. Nawojki 11, PO Box 386, PL-30-950, Kraków 23, Poland*

Accepted .... Received ....; in original form ...

## ABSTRACT

We report the results of a multifrequency campaign targeting S5 0716+714 in the flaring state of the source observed in 2015 January and February. The observations have been performed using the following instruments: *Fermi*/Large Area Telescope (LAT), *Nuclear Spectroscopic Telescope Array*, X-ray Telescope and Ultraviolet/Optical Telescope. The elevated flux level was visible in all frequencies and the outburst consists of five sub-flares. In this paper we focus on the analysis of the X-ray observations both in the soft and hard regimes for data collected with *NuSTAR* and *Swift*/XRT. This is the first time, when hard X-ray observations of the source collected with *NuSTAR* are reported. The studies reveal both low- and high-energy components clearly visible in the energy band, with the break energy of 8 keV, which is the highest break energy ever reported for S5 0716+714. The second part of this work is concentrated on multifrequency observations collected during the flaring activity period. The variability patterns recorded during the period are characterized using a fractional variability amplitude and description of the flare profiles. The correlation studies reveal strong and significant relation between the optical, ultraviolet and  $\gamma$ -ray observations, and no time lag is found for any of the studied relations.

**Key words:** radiation mechanisms: non-thermal – galaxies: active – BL Lacertae objects: general,

## 1 INTRODUCTION

Blazars, BL Lacertae (BL Lac) type objects and flat spectrum radio quasars (FSRQs), are an extreme class of active galactic nuclei, characterized with polarized and highly variable non-thermal emission observed from the jets pointing at small angles to the observer (e.g., Begelman et al. 1984). The emission is observed in a wide energy range from radio frequencies up to high and very high energy  $\gamma$ -ray regime (e.g. Vercellone et al. 2011; H.E.S.S. Collaboration 2013, 2014). The spectral energy distribution (SED) of blazars, in  $\nu$ - $\nu F_\nu$  representation, is characterized with a double-bumped shape. The first, low-energy bump usually is attributed to synchrotron radiation of relativistic electrons from the jet, while the origin of the high-energy bump is still debatable and can be explained in terms of both the leptonic and hadronic scenarios (see e.g. Maraschi et al. 1992; Mannheim 1993; Sikora et al. 1994; Kirk et al. 1998; Mücke et al. 2003; Böttcher et al. 2013). In the most popular

so-called Synchrotron-self-Compton model (SSC) this high-energy bump is a result of the inverse Compton scattering of the low energy photons collided with the highly energetic leptons.

The position of the low energy peak in blazars SED allows us to distinguish high-, intermediate- and low-energy peaked objects: HBL, IBL, LBL, respectively (see, e.g., Padovani & Giommi 1995; Fossati et al. 1998; Abdo et al. 2010a). For HBL type blazars the low energy peak is situated in the X-ray domain ( $\nu_s > 10^{15}$  Hz), for IBL blazars in the optical-ultraviolet (UV) range ( $10^{14}$  Hz  $< \nu_s \leq 10^{15}$  Hz), while in the case of LBL type blazars in the infrared regime ( $\nu_s \leq 10^{14}$  Hz) (Abdo et al. 2010a). Different subclasses of blazars FSRQs–LBLs–IBLs–HBLs form a blazar sequence which connects decreasing bolometric luminosities and  $\gamma$ -ray dominance in different group of sources (Fossati et al. 1998).

The blazar S5 0716+714 ( $z = 0.31$ ) (Nilsson et al. 2008), classified as an IBL type object (e.g. Giommi et al. 1999; Abdo et al. 2010a), is one of the brightest and most active blazar. The source was discovered in the 5 GHz Bonn-National Radio Astronomy Observatory radio survey and

\* E-mail: alicja.wierzcholska@ifj.edu.pl

† E-mail: h.siekowski@cyfronet.pl

included in S5 catalogue (Kuehr et al. 1981a). The object was a target of several optical campaigns focusing on intra-night variability (e.g. Wagner et al. 1996; Montagni et al. 2006; Gupta et al. 2009; Rani et al. 2011a; Gupta et al. 2012; Bhatta et al. 2013, 2015).

A few instruments monitored the object in the X-ray regime and revealed the spectral upturn, disentangling two spectral components located in this range (e.g. Ferrero et al. 2006; Foschini et al. 2006; Wierzcholska & Siejkowski 2015). The source is included in the first, second and third *Fermi*/LAT catalogues (1FGL, 2FGL, 3FGL, respectively Abdo et al. 2010b; Nolan et al. 2012; Acero et al. 2015) as well as in the *Fermi*/LAT Bright Source List (0FGL, Abdo et al. 2009), and the First *Fermi*/LAT Catalog of Sources Above 10 GeV (1FHL; Ackermann et al. 2013). In the very high energy  $\gamma$ -ray regime S5 0716+714 has been discovered with Major Atmospheric Gamma Imaging Cherenkov Telescopes (MAGIC) telescopes (Anderhub et al. 2009).

Rani et al. (2011b) studied multifrequency properties of S5 0716+714 during its various phases of activity using optical and radio observations. The authors find higher Doppler factors and higher synchrotron peak frequency for the source, when it is brighter.

Series of radio, optical, X-ray, and  $\gamma$ -ray observations of S5 0716+714 collected between 2007 April and 2011 January have been studied by Rani et al. (2013). The intensive monitoring reveals significant optical variability on time-scales of about 60–70 d. The optical activity is correlated with the one observed in the  $\gamma$ -ray regime, which supports SSC mechanism as responsible for the production of the high-energy emission. The optical and  $\gamma$ -ray emission is also correlated with the radio one, however in the X-ray regime an orphan flare has been observed, which makes one-zone model too simple to explain the activity observed.

Multi-wavelength observations including radio, optical, X-ray and  $\gamma$ -ray regimes in the studies by Liao et al. (2014) show significant variability in all bands. The highest variability amplitudes is observed in the optical and  $\gamma$ -ray regimes and lower in the X-ray and radio ones. The authors favour the SSC model with the external seed photons originating from the hot dust or broad line region as the best explanation for the emission observed.

In the more recent work, Chandra et al. (2015) studied multiwavelength properties of S5 0716+714 during the outburst in 2015 January. The authors report simultaneous optical, X-ray and  $\gamma$ -ray observations including a time-dependent modelling of the light curves. Furthermore, they find simultaneous variations in all observed bands. The studies support the leptonic origin of the high energy emission observed during the outburst.

This paper focuses on a flaring activity of the source observed in 2015 January–February. During the period mentioned the flaring state of the source was reported in different wavelengths: optical range (Bachev & Strigachev 2015; Bachev et al. 2015; Spiridonova et al. 2015), near-infrared regime (Carrasco et al. 2015), X-ray range (Wierzcholska & Siejkowski 2015) and very high energy  $\gamma$  rays regime (Mirzoyan 2015).

The paper is organized as follows: Section 2 describes the observations and the analysis procedures, Section 3 is focused on the monitoring of S5 0716+714 in soft and hard

X-ray band, in Section 4 the multifrequency variability patterns are studied. The work is summarized in Section 5.

## 2 OBSERVATIONS AND DATA ANALYSIS

### 2.1 *Fermi*-LAT observations

The *Fermi*/LAT is a pair-production satellite telescope sensitive to measure high energy  $\gamma$  rays from tens of MeV up to about 500 GeV (Atwood et al. 2009). The data collected between MJD57023 and MJD57078 in the energy range of 100 MeV and 300 GeV were analysed using standard `ScienceToolsv10r0p5` with `P8R2_SOURCE_V6` instrument response function. For the analysis events within  $10^\circ$  region of interest (ROI) centred on S5 0716+714 were selected. The binned maximum-likelihood method (Mattox et al. 1996) was applied in the analysis. The Galactic diffuse background was modelled using the `gll_iem_v06` map cube, and the extragalactic diffuse and residual instrument backgrounds were modelled jointly using the corresponding isotropic emission template. All sources from the *Fermi*-LAT Third Source Catalogue (Acero et al. 2015) inside the ROI of S5 0716+714 were modelled.

For the spectral analysis the same energy range as defined earlier was used. To find which model best describes the spectrum, three models: power-law (`PowerLaw`), log-parabola (`LogParabola`) and `PLSuperExpCutoff` has been fitted. The log-likelihoods of the fits are:  $-77938.7$ ,  $-77933.8$  and  $-77937.9$ , respectively. The comparison of the fit quality to the power-law model, according to the Wilks theorem (Wilks 1938), favours the log-parabola model with test-statistics (TS) equal to 9.7 and  $p$ -value to 0.002. In the case of the `PLSuperExpCutoff` model the TS is 1.5 and  $p$ -value = 0.214. Therefore for the further analysis the log-parabola model is chosen.

### 2.2 *NuSTAR* observations

The Nuclear Spectroscopic Telescope Array (*NuSTAR*) is a satellite instrument dedicated for observations in the hard X-ray regime (3–79 keV) (Harrison et al. 2013). It consists of two detectors (A and B), with a field of view of each telescope of about 13 arcmin. *NuSTAR* observed S5 0716+714 twice on 2015 January 24 with the exposures of 338 and 18583 s (ObsIDs: 90002003001 and 90002003002, respectively). In both cases the observations were performed in the `SCIENCE` mode. Due to very short exposure of the first pointing, in the further studies we focus on the second observation only. The raw data were processed with *NuSTAR* Data Analysis Software package (NUSTARDAS) version 1.4.1 (released as a part of HEASOFT 6.16) using standard `nupipeline` task. The data were processed with the most recent calibration version compatible with NUSTARDAS v.1.4.1 (version 20140414). A source region was selected within a circle with a radius of 0.5 arcmin centred on S5 0716+714. The same-size region was selected for a background area. In the spectral analysis, we focus on channels which correspond to energy range of 3–40 keV. The instrumental response matrices and effective area files were produced with `nuproducts` procedure. The count rate light curves for both telescopes are presented in Fig. 1. The subtracted background count

rate is  $0.228 \pm 0.005$  count/s and  $0.250 \pm 0.008$  count/s for A and B telescope, respectively. Hence, in the spectral fits small normalization factor for the module A with respect to the module B was taken into account. Fig. 1 does not reveal any significant variability during the observations and the count rate is constant within the error bars.

### 2.3 Swift-XRT observations

The Swift Gamma-Ray Burst Mission (hereafter *Swift*; Gehrels et al. 2004) is a multiwavelength space observatory. It is equipped with three instruments: the Burst Alert Telescope (BAT; Barthelmy et al. 2005), the X-ray Telescope (XRT; Burrows et al. 2005), and the Ultraviolet/Optical Telescope (UVOT; Roming et al. 2005). The *Swift*/BAT operates in the energy range of 15–150 keV, while *Swift*/XRT in the 0.3–10 keV range. *Swift*/UVOT observations are provided in six wavelengths covering the range of 170–600 nm.

X-ray data in the energy range of 0.3–10 keV collected with *Swift*/XRT were analysed using version 6.16 of the HEASOFT package<sup>1</sup>. Data were recalibrated using the standard procedure `xrtipeline`. For the spectral fitting XSPEC v.12.8.2 was used (Arnaud 1996). All data were binned to have at least 30 counts per bin. The light-curve points have been derived by fitting each single observation with a log-parabola model with a Galactic absorption value of  $N_{\text{H}} = 3.22 \times 10^{20} \text{ cm}^{-2}$  (Kalberla et al. 2005) set as a frozen parameter. The *Swift*/XRT data has been corrected for pile-up effect where needed.

### 2.4 Swift/UVOT observations

The UVOT instrument onboard *Swift* measures the UV and optical emission simultaneously with the X-ray telescope. The observations are taken in the UV and optical bands with the central wavelengths of: 188 nm (*UVW2*), 217 nm (*UVM2*), 251 nm (*UVW1*), 345 nm (*U*), 439 nm (*B*), and 544 nm (*V*). The instrumental magnitudes were calculated using `uvotsource` including all photons from a circular region with a radius of 5 arcsec. The background was determined from a circular region with a radius of 5 arcsec near the source region, not contaminated with any signal from the nearby sources. The flux conversion factors from Poole et al. (2008) were used. All data were corrected for the dust absorption using the reddening  $E(B-V) = 0.02557$  mag (Schlafly & Finkbeiner 2011) and the ratios of the extinction to reddening,  $A_{\lambda}/E(B-V)$ , for each filter provided by Giommi et al. (2006).

In order to estimate the influence of the host galaxy of S5 0716+714, the observations made by Nilsson et al. (2008) are used. They find that the host galaxy has *I*-band magnitude of  $17.5 \pm 0.5$  and an effective radius of  $(2.7 \pm 0.8)$  arcsec. The host galaxy of S5 0716+714 is assumed to be an elliptical galaxy and in order to find the magnitudes in other bands the templates provided by Fukugita et al. (1995) are used. The host galaxy magnitudes visible by *Swift*/UVOT aperture of 5 arcsec are  $m_V = 19.6$ ,  $m_B = 21.2$ ,  $m_U = 21.7$ . The maximal contribution of the host galaxy to the *Swift*/UVOT observations are then: 0.7, 0.3, and  $<0.1$  per cent in *V*, *B*

and *U* bands, respectively, therefore we find the correction for the host galaxy as negligible. All the measured magnitudes are collected in Table 1.

## 3 OBSERVATIONS IN THE X-RAY REGIME

During the multifrequency campaign S5 0716+714 was monitored in the X-ray regime with two instruments: *Swift*/XRT and *NuSTAR*. *Swift*/XRT observations with ObsIDs of 00035009154–00035009158 were taken with quasi-simultaneous *NuSTAR* data with ObsID of 90002003002. For the joint spectral fit, we consider *Swift*/XRT observations taken in the energy range of 0.3–10 keV and *NuSTAR* observations collected in the energy band of 3–50 keV. We note here that during the period of *Swift*/XRT quasi-simultaneous observations the variability was small. Unfortunately, there are not any ideally simultaneous *Swift*/XRT observations with the *NuSTAR* ones.

Three different models: a single power-law, a broken power-law and a log-parabola, as defined below, are fitted in order to find the best description of the X-ray observations. In each case we include the Galactic hydrogen absorption fixed as a frozen value  $N_{\text{H}} = 3.22 \times 10^{20} \text{ cm}^{-2}$  (Kalberla et al. 2005). We use following spectral models:

- a single power-law:

$$\frac{dN}{dE} = N_p \left( \frac{E}{E_0} \right)^{-\Gamma}, \quad (1)$$

with the spectral index  $\Gamma$  and the normalization  $N_p$ ,

- a logarithmic parabola:

$$\frac{dN}{dE} = N_l \left( \frac{E}{E_0} \right)^{-(\alpha + \beta \log(E/E_0))}, \quad (2)$$

with the normalization  $N_l$ , the spectral parameter  $\alpha$  and the curvature parameter  $\beta$ ,

- a broken power-law:

$$\frac{dN}{dE} = N_b \times \begin{cases} (E/E_b)^{-\Gamma_1} & \text{if } E < E_b, \\ (E/E_b)^{-\Gamma_2} & \text{otherwise,} \end{cases} \quad (3)$$

with the normalization  $N_b$ , the spectral indices  $\Gamma_1$  and  $\Gamma_2$  and the break energy  $E_b$ .

In the case of the power-law and log-parabola models the scale energy  $E_0$  is fixed at 1 keV. Since *Swift*/XRT and *NuSTAR* are not ideally simultaneous, in every case mentioned 2% of systematic errors are added to the data points. All the fits parameters are collected in Table 2, and the spectral fits with residuals and the corresponding SEDs are shown in Fig. 2. Based on the  $\chi^2_{\text{red}}$  values and the residual distribution, we conclude that the single power-law model with a fixed value of the Galactic absorption is not sufficient to describe the X-ray spectrum. We also test the power-law model with free  $N_{\text{H}}$  value, which results in lower  $\chi^2_{\text{red}}$  value, i.e.  $\chi^2_{\text{red}} = 1.574$  and  $\chi^2_{\text{red}} = 1.318$  for the power-law with Leiden/Argentine/Bonn Survey and free  $N_{\text{H}}$ , respectively. The fit with free  $N_{\text{H}}$  results in  $N_{\text{H}}^{\text{free}} \sim 10^{15} \text{ cm}^{-2}$  which is significantly smaller than the one provided by Kalberla et al. (2005).

The *F*-test (e.g. Bevington & Robinson 2003) shows significant improvement of the broken power-law and log-parabola models relative to the power-law model, and the corresponding *p*-values are  $> 10^{-8}$  in both cases. However,

<sup>1</sup> <http://heasarc.gsfc.nasa.gov/docs/software/lheasoft>

it is difficult to distinguish between those two concave models hence we conclude that the broken power-law and log-parabola models both describes the X-ray spectra very well. It is also worth mentioning here that for both cases: the broken power-law and log-parabola model reveal larger residua around 10 keV. It is more pronounced in the first case. This may be caused by the fact that the spectrum consists of data collected with two different instruments *Swift*/XRT and *NuSTAR*. Furthermore, data are not strictly simultaneous and even within *NuSTAR* data set marginal variations are present.

Since the log-parabola is described with a significantly negative curvature, we then conclude that the X-ray regime reveals both the low- and the high-energy spectral components, with the highest break energy value, ever reported for this source, of about 8 keV.

To compare the X-ray spectra with the observation in the optical and  $\gamma$ -ray regimes the broad-band SED in the  $\nu$ - $F_\nu$  representation is shown in Fig. 3. The optical data are the mean values of the *Swift*/UVOT observations and the error bars show the standard deviation. The  $\gamma$ -ray observations are the *Fermi*/LAT data and the parameters of the log-parabola fit are following, the normalization is  $(2.07 \pm 0.05) \times 10^{-10} \text{ cm}^{-2} \text{ s}^{-1} \text{ MeV}^{-1}$ ,  $\alpha = 1.92 \pm 0.02$  and  $\beta = 0.03 \pm 0.01$ . The spectral points in the gamma-ray regime are generated by dividing the range analysed into five bins and by fitting the power-law model for each separately. The plot is supplemented with the archive data taken from ASDC<sup>2</sup> and includes observations of the following regimes: radio (Kuehr et al. 1981b; White & Becker 1992; Gregory et al. 1996; Cohen et al. 2007), infrared (Wright et al. 2010; Planck Collaboration et al. 2011, 2014) and very high energy (VHE)  $\gamma$ -ray (Anderhub et al. 2009).

#### 4 TEMPORAL VARIABILITY

The long-term light curve including data collected with *Fermi*/LAT, *Swift*/XRT, *Swift*/UVOT is presented in Fig. 4. The source is active in all the regimes presented. First look on the light curves suggests that flaring activity of the blazars is different in another regimes. These aspects are widely discussed in Section 4.1, but it is worth mentioning here that the optical observations of S5 0716+714 with *Swift*/UVOT in *U*, *B*, and *V* filter are saturated and only lower limits are given in Table 1 and presented in Fig. 4. These observations correspond to the highest flux points in the UV bands, which are not saturated. We exclude these optical observations from the further calculations.

In order to quantify a temporal variability of S5 0716+714, the fractional variability amplitude is calculated following the definition by Vaughan et al. (2003):

$$F_{\text{var}} = \sqrt{\frac{S^2 - e^2}{F^2}}, \quad (4)$$

where  $S^2$  is the variance,  $e^2$  is the mean square error, and  $F$  is the mean flux. The uncertainties of  $F_{\text{var}}$  are calculated following the formula by Poutanen et al. (2008):

$$\delta F_{\text{var}} = \sqrt{F_{\text{var}}^2 + (\sigma^2)} - F_{\text{var}}, \quad (5)$$

with the error in the normalized excess variance  $\sigma$  given as (Vaughan et al. 2003)

$$\sigma = \sqrt{\left(\sqrt{\frac{2}{N} \frac{e^2}{F^2}}\right)^2 + \left(\sqrt{\frac{e^2}{N} \frac{2F_{\text{var}}}{F}}\right)^2}, \quad (6)$$

where  $N$  is the number of data points in the light curve. Results for different frequencies are collected in Table 3 and presented in Fig. 5. The blazar is highly variable in the UV regime. In the optical bands calculated  $F_{\text{var}}$  is lower than for the case of UV observations. We remind here that the highest optical observations are given only as lower limits and excluded from the calculation, hence the lower  $F_{\text{var}}$ . The lowest  $F_{\text{var}}$  value is found for the X-ray observations.

It must be noted here that  $F_{\text{var}}$  strongly depends on the sampling and size of the time bins. In the case of the current analysis the sampling in *Fermi*/LAT and *Swift*/XRT are different, i.e. *Fermi*/LAT has a regular sampling as opposed to *Swift*/XRT. The size of the time bins influences the  $F_{\text{var}}$  by smoothing out the variability, and lowering its values in the case of larger time bins. Obviously, the time binning is related to the characteristics of the instrument, sensitivity in particular. Another key factor are the flux uncertainties, which according to the definition of  $F_{\text{var}}$  should be constant or at least very close to it. In our analysis this requirement is not strictly fulfilled, however the flux uncertainties are very similar in given energy band.

Since a few significant flares can be distinguished during time of the outburst, we aim to analyse the individual outbursts in different energy regimes. The individual flares are defined in Table 4. The flux evolution during the flaring event can be characterized using a function, which describes the time profiles of a single flare (Abdo et al. 2010c):

$$F(t) = F_e + \frac{F_0}{e^{\frac{t_0-t}{T_r}} + e^{\frac{t-t_0}{T_d}}}, \quad (7)$$

where  $F_e$  represents the constant flux level underlying the flare,  $F_0$  is the amplitude of the flare,  $t_0$  is the time of the peak and  $T_r$  and  $T_d$  represent the rise and decay times, respectively. The time of the peak position  $t_m$  is calculated using the following formula:

$$t_m = t_0 + \frac{T_r T_d}{T_r + T_d} \ln \left( \frac{T_r}{T_d} \right). \quad (8)$$

The symmetry of the flare can be described as:

$$\xi = \frac{T_d - T_r}{T_d + T_r}, \quad (9)$$

which can be between  $-1$  and  $1$ . The border limits correspond to completely the right and left asymmetric flares, respectively.

In this paper, the fitting procedure is limited to the following rules:

- (i) in the case of the UV observations we focus on four main outbursts visible; fitting procedure is performed on data collected in *UVW2* band;
- (ii) in the case of the optical observations we focus on four main outbursts visible; fitting procedure is performed on data collected in *U* band and the upper limit points are not taken into account during the fitting procedure;

<sup>2</sup> <http://tools.asdc.asi.it/SED/>

- (iii) in the case of the X-ray observations only the observations taken in Windowed Timing (WT) mode are used, which makes possible to fit only two flares;
- (iv) in the case of the  $\gamma$ -ray observations only two significant flares are distinguished and fitted.

The exact dates of the flares selected as well as the fit parameters are listed in Table 4.

All of the flares in given wavelengths are asymmetric, and both, right and left, asymmetries are found. We denote the flares by A–E symbols (also given in Table 4) in order to distinguish the simultaneous flares in the further discussion.

- (i) Flare A is observed only with *Fermi*/LAT and there is no information about the flux level observed in other wavelengths.
- (ii) Flare B is observed with *Swift*/UVOT both in the optical and UV bands. The fitted shapes of this outburst in both cases, show weak right asymmetry.
- (iii) Flare C is revealed with *Swift*/UVOT, *Swift*/XRT, and *Fermi*/LAT. In every fit, the shape reveals left asymmetry, and the effect is the strongest for the X-ray data.
- (iv) Flare D is observed in the UV, optical and X-ray regimes. The observations reveal right asymmetry for this outburst.
- (v) Flare E is observed with *Swift*/UVOT in the optical and UV regimes. The value of the asymmetry coefficient strongly suggests right asymmetry in the case of this outburst.

The outbursts observed are characterized with not only different asymmetries, but also with different duration times. The duration of the flares, calculated as a sum of the rise and decay times, is between 2.33 and 6.25 d. It is also worth mentioning that the duration time of a given flare differs between regimes.

#### 4.1 Correlation studies

To find a relation between the emissions observed on different wavelengths a cross-correlation function (CCF) is used. The CCF function is estimated using the  $z$ -transformed discrete correlation function (ZDCF) following the algorithm described in detail by Alexander (1997). Furthermore a maximum-likelihood is calculated for each case using the PLIKE algorithm (Alexander 2013) in order to find the peak location for the ZDCF. This peak location,  $\tau_{\max}$ , represents the most probable timelag between the two light curves compared. For each pair of the light curves the  $\tau_{\max}$  and the Pearson correlation coefficient for the given light curves shifted according to the  $\tau_{\max}$  are calculated, as well as the likelihood of the time lag. The results are gathered in Table 5. Every CCF function between the optical and UV bands give a single and strong likelihood peak for the time lag equals to zero (within the uncertainties), therefore the values are not reported in the table. This can be also verified visually by looking at the light curves in Fig. 4.

The cross-correlation of *Swift*/XRT and *Fermi*/LAT data results in three time lags (see Fig. 6). The flare B is not well sampled in the X-ray observations. This strongly influences the calculated ZDCF values, therefore the found time lags of about 11, 18, and 21 d might be the local maxima.

The time distances, between flare B and C is around 10.5 d and between B and D is 19.6 d, and these values correlate with the time lags calculated. Assuming that the flare B for the *Swift*/XRT observations would be more pronounced (similarly as for optical/UV observations), and taking into account that the maximum flux for *Fermi*/LAT data is around flare B this could result in strong correlation for time lag equals to zero or a value close to it. Therefore the found time lags of 11, 18, and 21 d could be simply artefacts.

For the comparison of *Swift*/UVOT and *Fermi*/LAT observations, we find two significant correlations for the  $U$  and  $V$  filters and one in the case of the  $B$  filter. In every case, the time lags are with the uncertainties close to zero days. Similar situation is in the case of the UV observations. We do not find any other significant time lag, except for zero days. Please note that *Fermi*/LAT data are binned in 1 d long intervals and therefore the calculation of the time lags can be slightly disturbed.

#### 5 SUMMARY AND CONCLUSIONS

S5 0716+714 is a highly variable blazar and it was monitored in multiple regimes with different instruments (e.g. Chen et al. 2008; Liao et al. 2014; Chandra et al. 2015), but in this paper for the first time, hard X-ray observations collected with *NuSTAR* are studied. The paper focuses on the X-ray monitoring of the blazar during its flaring state in 2015 January. The previous soft X-ray campaigns targeting S5 0716+714 has revealed that this regime is a place, where both low- and high-energy components meet. It is also worth mentioning that during different epochs of observations and different states of the blazars the break energy shifts between 1.5 and 5.3 keV (Tagliaferri et al. 2003; Donato et al. 2005; Ferrero et al. 2006; Wierzcholska & Siejkowski 2015).

This is the first time, when the soft and hard X-ray observations of S5 0716+714 are studied together. The joint spectral fit to *Swift*/XRT and *NuSTAR* data confirms a concave shape and existence of the low- and high-energy components in the X-ray energy regime. The shape of the spectrum within the energy range of 0.3–40 keV is well constrained and the log-parabola or broken power-law models are the preferable models to describe the X-ray spectrum. The low-energy component is characterized by a spectral index in the range of about 2.4–2.5, depending on the model. We found the break energy – a point where both components meet – at about 8 keV. This is the highest break energy ever reported for S5 0716+714.

The second part of this paper is concentrated on the multifrequency observations of S5 0716+714 with *Fermi*/LAT, *NuSTAR*, *Swift*/XRT, and *Swift*/UVOT. The flaring activity is observed in every regime, and five sub-flares can be resolved in different regimes. The flaring activity of S5 0716+714 is characterized with the fractional variability amplitudes. The shape of the flares in different energy regimes is also characterized with a rise and decay times and asymmetry coefficient. These studies have shown that between and within the energy bands the flares are characterized with different values of the rise and decay times and also different asymmetry coefficients. We did not find any pattern behaviour for the flares described, but the same flares observed in different energy regimes have very simi-

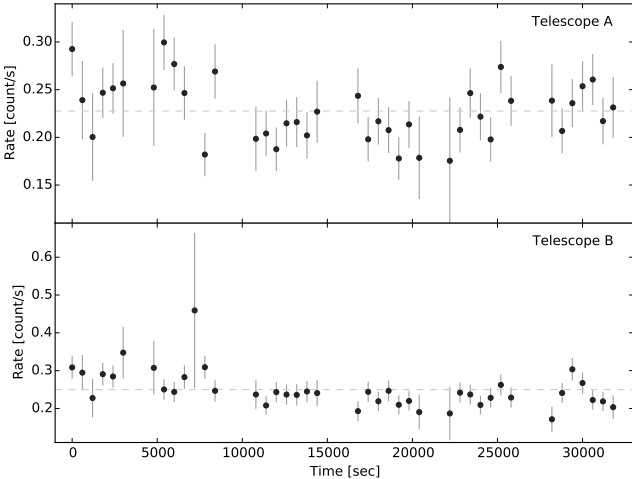


**Figure 1.** The X-ray count rate light curve measured with *NuSTAR*. Data points are binned in 600 s intervals. The upper panel presents data collected with telescope A, while the bottom one with telescope B.

lar characteristics, including the asymmetry coefficients. No significant shifts between the peak positions of the flares observed in different wavelengths are found.

The correlation studies reveal strong positive correlation for the optical and UV observations for all of the energy band combinations. We also found such a relation for a comparison of  $\gamma$ -ray and optical data, and for  $\gamma$ -ray and UV data. In each case, the calculated value of a time lag is zero days or very close to it. We did not find any significant relation for a comparison of the X-ray observations with other wavelengths, except for the *Fermi*/LAT data, but the results are probably artefacts due to the mismatched sampling of the *Swift*/XRT and *Fermi*/LAT data.

The correlations suggest that the UV, optical and  $\gamma$ -ray emission observed may origin from the same emission region. We have shown that the asymmetry of any particular flare is the same for different frequencies and the duration of the flare is shortening with the increasing energy. The results strengthen the hypothesis that the emission origins from the same region.

## ACKNOWLEDGEMENTS

The authors thank anonymous referee for suggestions and remarks provided. This research was supported in part by PLGrid Infrastructure. The plots presented in this paper are rendered using MATPLOTLIB (Hunter 2007).

## REFERENCES

Abdo A. A. et al., 2010a, *ApJ*, 716, 30  
 Abdo A. A. et al., 2010b, *ApJS*, 188, 405  
 Abdo A. A. et al., 2010c, *ApJ*, 722, 520  
 Abdo A. A. et al., 2009, *ApJS*, 183, 46  
 Acero F., Ackermann M., Ajello M., Albert A., Atwood W. B., 2015, *ApJS*, 218, 23  
 Ackermann M. et al., 2013, *ApJS*, 209, 34  
 Alexander T., 1997, in *Astrophysics and Space Science Library*, Vol. 218, *Astronomical Time Series*, Maoz D., Sternberg A., Leibowitz E. M., eds., p. 163  
 Alexander T., 2013, ArXiv e-prints, 1302.1508  
 Anderhub H. et al., 2009, *ApJ*, 704, L129  
 Arnaud K. A., 1996, in *Astronomical Society of the Pacific Conference Series*, Vol. 101, *Astronomical Data Analysis Software and Systems V*, Jacoby G. H., Barnes J., eds., p. 17  
 Atwood W. B. et al., 2009, *ApJ*, 697, 1071  
 Bachev R., Spassov B., Boeva S., 2015, *The Astronomer's Telegram*, 6944, 1  
 Bachev R., Strigachev A., 2015, *The Astronomer's Telegram*, 6957, 1  
 Barthelmy S. D. et al., 2005, *Space Sci. Rev.*, 120, 143  
 Begelman M. C., Blandford R. D., Rees M. J., 1984, *Reviews of Modern Physics*, 56, 255

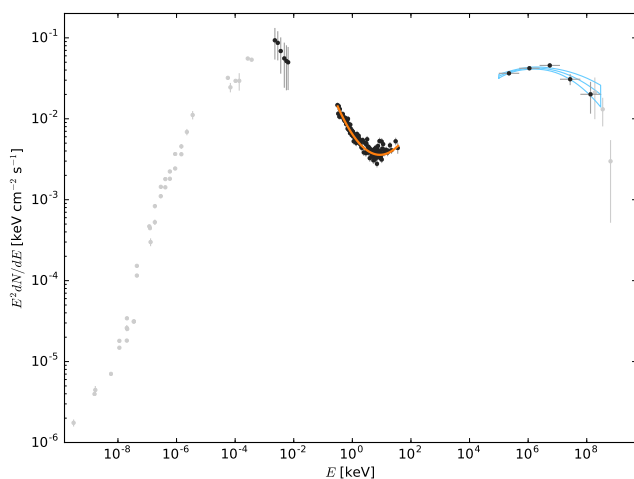


**Figure 3.** The broad-band SED plot. The black dots show the optical, UV, X-ray and  $\gamma$ -ray observations collected with *Swift*/UVOT, *Swift*/XRT, *NuSTAR*, and *Fermi*/LAT. The error bars of the optical data show the standard deviation. The grey points show archive observations (the references are given in text).

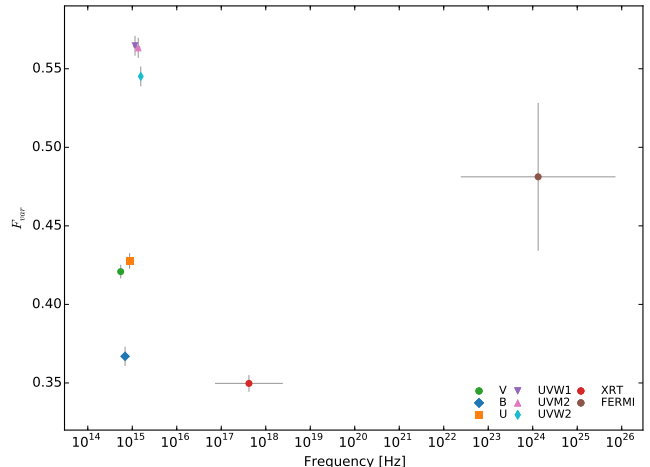


**Figure 5.** The fractional variability amplitudes for different frequencies.

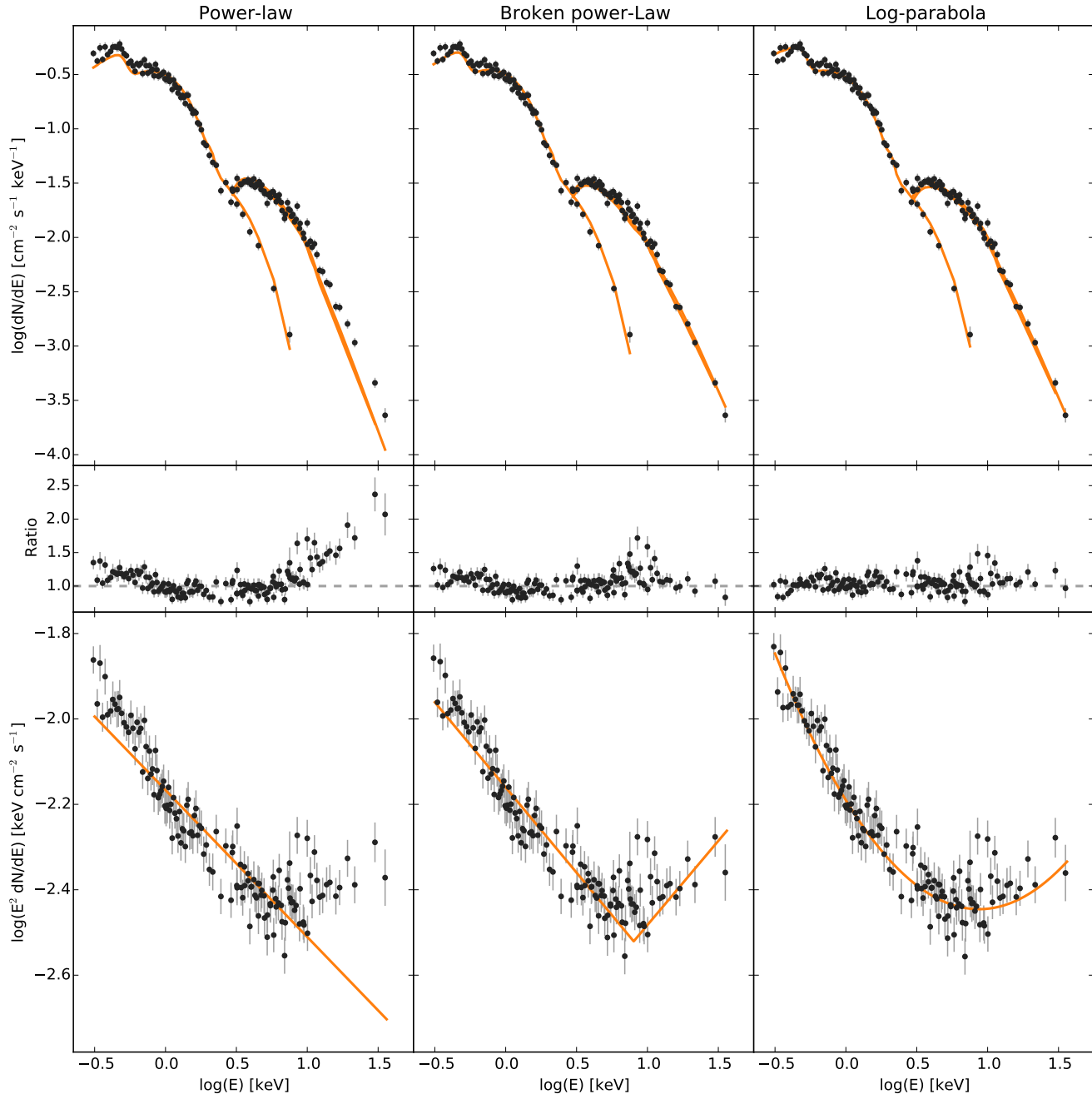


**Figure 2.** The spectral fits for S5 0716+714. The upper panels present the spectral points and the fitted model for the three tested models: power-law, broken power-law, and log-parabola. The middle panel presents the corresponding ratios, while the lower ones show data and the fitted models of the SEDs for power-law, broken power-law, and log-parabola model, respectively.

Bevington P., Robinson D., 2003, Data reduction and error analysis for the physical sciences, McGraw-Hill Higher Education. McGraw-Hill, Boston, MA

Bhatta G. et al., 2015, ArXiv e-prints (1507.08424)

Bhatta G. et al., 2013, A&A, 558, A92

Böttcher M., Reimer A., Sweeney K., Prakash A., 2013, ApJ, 768, 54

Burrows D. N. et al., 2005, Space Sci. Rev., 120, 165

Carrasco L., Porras A., Recillas E., Leon-Tavares J., Chavushyan V., Carraminana A., 2015, The Astronomer's Telegram, 6902, 1

Chandra S., Zhang H., Kushwaha P., Singh K. P., Bottcher M., Kaur N., Balyan K. S., 2015, ArXiv e-prints (1507.06473)

Chen A. W. et al., 2008, A&A, 489, L37

Cohen A. S., Lane W. M., Cotton W. D., Kassim N. E., Lazio T. J. W., Perley R. A., Condon J. J., Erickson W. C., 2007, AJ, 134, 1245

Donato D., Sambruna R. M., Gliozzi M., 2005, A&A, 433, 1163

Ferrero E., Wagner S. J., Emmanoulopoulos D., Ostorero L., 2006, A&A, 457, 133

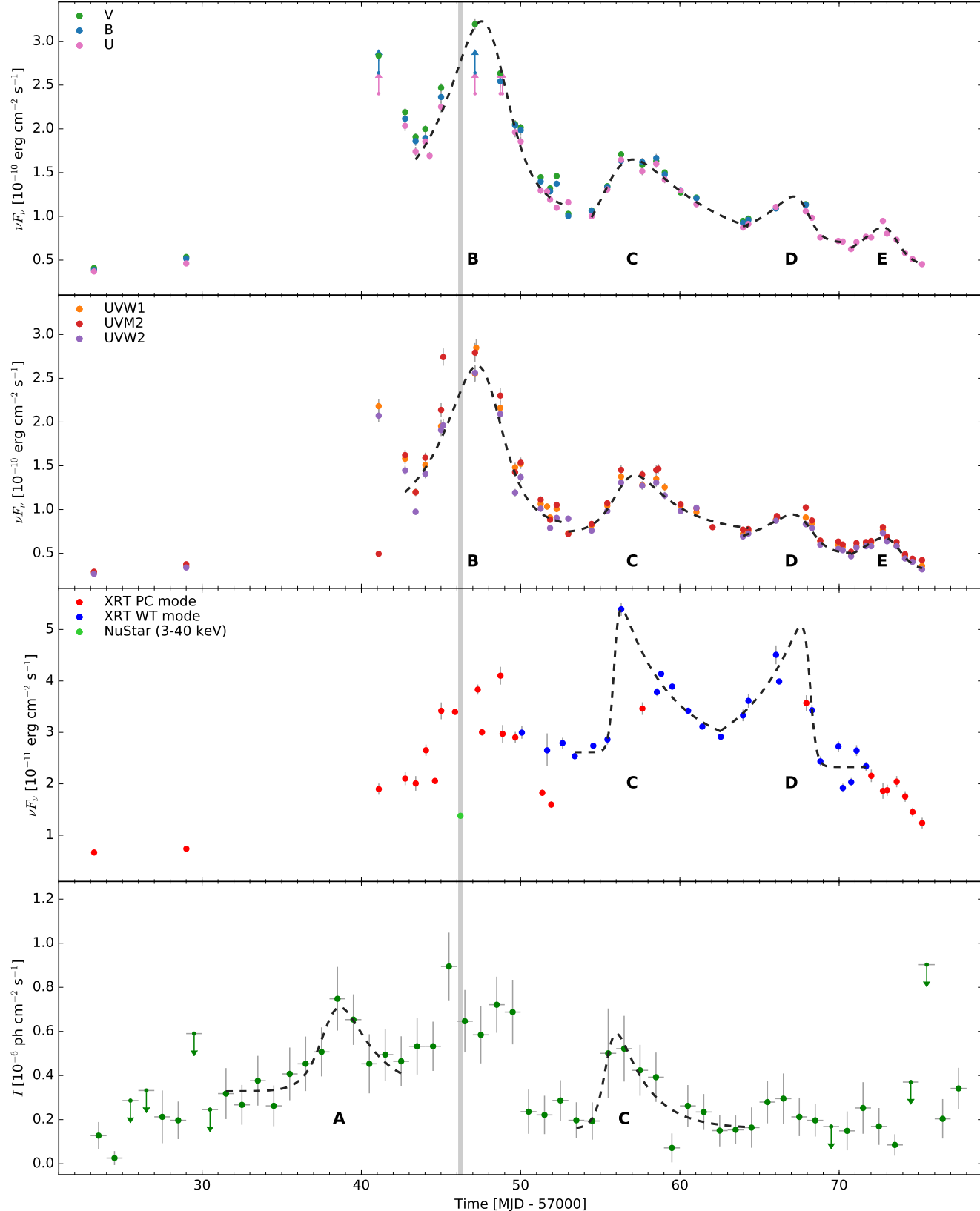


**Figure 4.** The light curves of S5 0716+714. The following panels (from top to bottom) show: the optical and UV observations with *Swift*/UVOT, the *Swift*/XRT and *NuSTAR* monitoring, and  $\gamma$ -ray data gathered with *Fermi*/LAT. The letters A–E mark the flares defined in Table 4 and the dashed lines show the fits of the flare profile. The vertical shaded line indicates time of the *NuSTAR* observation.

**Table 1.** Magnitudes for different epochs from *Swift*/UVOT data for *V*, *B*, *U*, *UVW1*, *UVM2*, and *UVW2* filters.

Observation ID	Date	<i>U</i>	<i>B</i>	<i>V</i>	<i>UVW1</i>	<i>UVM2</i>	<i>UVW2</i>
00035009145	2015-01-01 05:04:59	13.94±0.05	14.76±0.05	14.31±0.05	14.09±0.06	14.14±0.06	14.30±0.06
00035009146	2015-01-07 00:04:59	13.70±0.05	14.45±0.05	14.02±0.05	13.84±0.06	13.86±0.06	14.04±0.06
00035009147	2015-01-19 02:05:48	<11.91	<12.68	12.21±0.04	11.87±0.05	13.56±0.05	12.07±0.05
00035009148	2015-01-20 17:54:59	12.09±0.05	12.92±0.05	12.49±0.04	12.22±0.05	12.27±0.05	12.46±0.05
00035009149	2015-01-21 09:44:59	12.29±0.05	13.06±0.05	12.64±0.04	12.52±0.05	12.60±0.05	12.89±0.05
00035009152	2015-01-22 00:22:59	12.19±0.05	13.04±0.04	12.59±0.04	12.27±0.05	12.29±0.05	12.49±0.05
00035009153	2015-01-22 06:51:59	12.29±0.04	—	—	—	—	—
00035009154	2015-01-23 00:08:59	11.98±0.05	12.80±0.05	12.36±0.04	11.99±0.05	11.97±0.05	12.16±0.05
00035009156	2015-01-23 03:20:58	—	—	—	—	11.70±0.05	—
00035009157	2015-01-25 03:13:59	<11.91	<12.68	12.08±0.04	11.70±0.05	11.68±0.06	11.84±0.05
00035009158	2015-01-25 05:09:59	—	—	—	11.58±0.05	—	—
00035009159	2015-01-26 17:21:48	<11.91	12.72±0.05	12.29±0.04	11.88±0.05	11.89±0.05	12.06±0.05
00035009160	2015-01-26 20:33:58	<11.91	—	—	—	—	—
00035009161	2015-01-27 15:42:46	12.13±0.05	12.96±0.05	12.56±0.04	12.29±0.05	12.41±0.05	12.67±0.05
00035009162	2015-01-28 00:08:58	12.19±0.05	12.99±0.05	12.58±0.04	12.26±0.06	12.33±0.06	12.52±0.05
00035009167	2015-01-29 06:13:59	12.58±0.05	13.37±0.05	12.94±0.04	12.65±0.05	12.68±0.05	12.85±0.05
00035009164	2015-01-29 15:52:21	12.59±0.05	—	—	—	—	—
00035009168	2015-01-29 20:24:58	12.67±0.05	13.46±0.05	13.04±0.04	12.82±0.05	12.93±0.05	13.12±0.05
00035009169	2015-01-30 06:21:59	12.76±0.04	13.39±0.04	12.93±0.04	12.71±0.05	12.74±0.05	12.97±0.05
00035009170	2015-01-30 23:47:59	12.70±0.04	13.73±0.04	13.31±0.04	13.06±0.05	13.15±0.06	12.98±0.05
00035009171	2015-02-01 10:59:58	12.86±0.05	13.67±0.04	13.27±0.04	12.93±0.05	12.99±0.05	13.16±0.05
00035009172	2015-02-02 10:38:59	12.57±0.05	13.42±0.05	13.02±0.04	12.67±0.05	12.72±0.05	12.88±0.05
00035009173	2015-02-03 07:23:59	12.32±0.05	13.20±0.05	12.76±0.04	12.37±0.05	12.39±0.06	12.57±0.05
00035009174	2015-02-04 15:17:20	12.41±0.05	13.21±0.05	12.84±0.04	12.45±0.05	12.43±0.05	12.60±0.05
00035009175	2015-02-05 12:23:59	12.35±0.05	13.18±0.05	12.81±0.04	12.39±0.05	12.39±0.06	12.57±0.05
00035009176	2015-02-05 15:34:59	—	—	—	—	12.38±0.05	—
00035009177	2015-02-06 01:09:59	12.48±0.05	13.31±0.04	12.90±0.04	12.47±0.05	—	12.70±0.05
00035009178	2015-02-07 01:06:00	12.58±0.04	13.45±0.04	13.08±0.04	12.67±0.05	12.73±0.05	12.88±0.05
00035009179	2015-02-08 00:55:00	12.72±0.05	13.53±0.04	13.13±0.04	12.75±0.05	12.78±0.05	12.84±0.05
00035009180	2015-02-09 01:15:59	—	—	—	—	13.04±0.06	—
00035009181	2015-02-10 22:59:59	13.01±0.05	13.82±0.05	13.40±0.04	13.07±0.05	13.08±0.06	13.26±0.05
00035009182	2015-02-11 07:09:58	12.96±0.05	13.78±0.05	13.37±0.04	13.02±0.06	13.07±0.06	13.21±0.05
00035009184	2015-02-13 00:42:30	12.75±0.05	13.64±0.05	—	12.85±0.05	—	13.01±0.05
00035009185	2015-02-13 02:08:43	—	—	—	—	12.88±0.05	—
00035009186	2015-02-13 02:24:59	—	—	—	—	12.89±0.05	—
00035009190	2015-02-14 21:45:05	12.80±0.05	13.60±0.05	13.20±0.04	12.82±0.05	12.77±0.05	13.06±0.07
00035009187	2015-02-15 06:54:58	12.88±0.05	—	—	13.91±0.05	12.94±0.06	13.12±0.05
00035009188	2015-02-15 19:34:59	13.16±0.05	—	—	13.20±0.06	13.27±0.06	13.42±0.05
00035009189	2015-02-16 22:45:58	13.22±0.05	—	—	13.28±0.05	13.29±0.06	13.51±0.05
00035009192	2015-02-17 05:21:59	13.23±0.05	—	—	13.32±0.05	13.35±0.06	13.54±0.05
00035009193	2015-02-17 17:58:59	13.37±0.05	—	—	13.48±0.06	13.51±0.06	13.69±0.06
00035009194	2015-02-18 02:02:59	13.24±0.05	—	—	13.31±0.06	13.32±0.06	13.48±0.05
00035009195	2015-02-18 16:24:59	13.15±0.05	—	—	13.27±0.05	13.30±0.06	13.45±0.05
00035009196	2015-02-19 00:14:59	13.16±0.05	—	—	13.23±0.06	13.28±0.06	13.45±0.05
00035009197	2015-02-19 17:54:59	12.92±0.05	—	—	13.01±0.06	13.04±0.06	13.20±0.06
00035009198	2015-02-20 00:10:59	13.10±0.05	—	—	13.16±0.05	13.20±0.06	13.35±0.05
00035009199	2015-02-20 14:32:59	13.20±0.05	—	—	13.29±0.06	13.30±0.06	13.45±0.05
00035009200	2015-02-21 03:18:59	13.45±0.05	—	—	13.53±0.06	13.57±0.06	13.75±0.05
00035009201	2015-02-21 14:29:59	13.59±0.05	—	—	13.65±0.06	13.69±0.06	13.85±0.05
00035009202	2015-02-22 04:56:58	13.72±0.05	—	—	13.84±0.06	13.73±0.06	14.11±0.06

Foschini L. et al., 2006, A&amp;A, 455, 871

Fossati G., Maraschi L., Celotti A., Comastri A., Ghisellini G., 1998, MNRAS, 299, 433

Fukugita M., Shimasaku K., Ichikawa T., 1995, PASP, 107, 945

Gehrels N. et al., 2004, ApJ, 611, 1005

Giommi P. et al., 2006, A&amp;A, 456, 911

Giommi P. et al., 1999, A&amp;A, 351, 59

Gregory P. C., Scott W. K., Douglas K., Condon J. J., 1996, ApJS, 103, 427

Gupta A. C. et al., 2012, MNRAS, 425, 1357

Gupta A. C., Srivastava A. K., Wiita P. J., 2009, ApJ, 690, 216

Harrison F. A. et al., 2013, ApJ, 770, 103

H.E.S.S. Collaboration, 2013, A&amp;A, 554, A107

H.E.S.S. Collaboration, 2014, A&amp;A, 571, A39

Hunter J. D., 2007, Computing In Science &amp; Engineering, 9, 90

Kalberla P. M. W., Burton W. B., Hartmann D., Arnal E. M., Bajaja E., Morras R., Pöppel W. G. L., 2005, A&amp;A,

**Table 2.** Results of the joint spectral fits to the *Swift*/XRT and *NuSTAR* observations in the X-ray range. The following columns present: (1) the chosen model: power-law, broken power-law or log-parabola; (2) the normalization given in  $10^{-3} \text{ cm}^{-2} \text{ s}^{-1} \text{ keV}^{-1}$ ; (3) the photon index for the power-law and log-parabola model, or the low-energy photon index for the broken power-law model; (4) the high-energy photon index for the broken power-law model, or the curvature parameter for the log-parabola model; (5) the break energy for the broken power-law model given in keV; (6) the unabsorbed model flux in the energy range of 2–10 keV; (7) the unabsorbed model flux in the energy range of 10–20 keV; (8) the unabsorbed model flux in the energy range of 20–50 keV; (9) the reduced  $\chi^2$  value and the number of degrees of freedom. The values for (6–8) are given in  $10^{-12} \text{ erg cm}^{-2} \text{ s}^{-1}$ .

Model (1)	Normalization (2)	$\Gamma/\Gamma_1/\alpha$ (3)	$\Gamma_2/\beta$ (4)	$E_{\text{br}}$ (5)	$F_{2-10}$ (6)	$F_{10-20}$ (7)	$F_{20-50}$ (8)	$\chi^2(\text{dof})$ (9)
power-law	$6.815 \pm 0.068$	$2.344 \pm 0.008$	–	–	$10.58 \pm 0.10$	$3.04 \pm 0.02$	$3.05 \pm 0.05$	1.574(513)
broken power-law	$6.912 \pm 0.067$	$2.399 \pm 0.009$	$1.606 \pm 0.053$	$8.01 \pm 0.56$	$10.03 \pm 0.10$	$4.19 \pm 0.02$	$7.64 \pm 0.37$	1.197(511)
log-parabola	$6.450 \pm 0.067$	$2.543 \pm 0.013$	$-0.289 \pm 0.016$	–	$10.04 \pm 0.01$	$4.13 \pm 0.16$	$6.58 \pm 0.29$	1.041(512)

**Table 3.** The fractional variability for different energy bands. The following columns present: (1) the name of the instrument, (2) the energy band or filter, (3) the fractional variability, and (4) the  $\chi^2$  value and the number of degrees of freedom for the fit with a constant.

Instrument (1)	Energy band/filter (2)	$F_{\text{var}}$ (3)	$\chi^2/n_{\text{dof}}$ (4)
<i>Fermi</i> /LAT	0.1 – 500 GeV	$0.4812 \pm 0.0471$	288/48
<i>Swift</i> /XRT	2 – 10 keV	$0.3497 \pm 0.0053$	8 562/60
<i>Swift</i> /UVOT	<i>UVW2</i>	$0.5451 \pm 0.0063$	18 193/42
<i>Swift</i> /UVOT	<i>UVM2</i>	$0.5633 \pm 0.0064$	14 800/44
<i>Swift</i> /UVOT	<i>UVW1</i>	$0.5646 \pm 0.0063$	18 233/43
<i>Swift</i> /UVOT	<i>U</i>	$0.4277 \pm 0.0050$	17 836/40
<i>Swift</i> /UVOT	<i>B</i>	$0.3669 \pm 0.0061$	14 572/25
<i>Swift</i> /UVOT	<i>V</i>	$0.4209 \pm 0.0044$	27 355/26

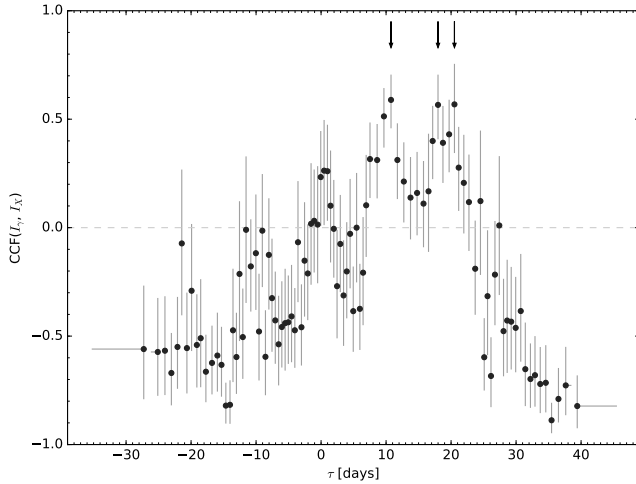


**Figure 6.** The CCF of the *Fermi*/LAT ( $I_{\gamma}$ ) and *Swift*/XRT ( $I_X$ ) light curves estimated using the ZDCF algorithm. The black arrows marks the maxima reported in Table 5.

440, 775  
 Kirk J. G., Rieger F. M., Mastichiadis A., 1998, A&A, 333, 452  
 Kuehr H., Pauliny-Toth I. I. K., Witzel A., Schmidt J., 1981a, AJ, 86, 854  
 Kuehr H., Witzel A., Pauliny-Toth I. I. K., Nauber U., 1981b, A&AS, 45, 367  
 Liao N. H., Bai J. M., Liu H. T., Weng S. S., Chen L., Li F., 2014, ApJ, 783, 83  
 Mannheim K., 1993, A&A, 269, 67

Maraschi L., Ghisellini G., Celotti A., 1992, ApJ, 397, L5  
 Mattox J. R. et al., 1996, ApJ, 461, 396  
 Mirzoyan R., 2015, The Astronomer's Telegram, 6999, 1  
 Montagni F., Maselli A., Massaro E., Nesci R., Sclavi S., Maesano M., 2006, A&A, 451, 435  
 Mücke A., Protheroe R. J., Engel R., Rachen J. P., Stanev T., 2003, Astroparticle Physics, 18, 593  
 Nilsson K., Pursimo T., Sillanpää A., Takalo L. O., Lindfors E., 2008, A&A, 487, L29  
 Nolan P. L. et al., 2012, ApJS, 199, 31  
 Padovani P., Giommi P., 1995, ApJ, 444, 567  
 Planck Collaboration et al., 2014, A&A, 571, A28  
 Planck Collaboration et al., 2011, A&A, 536, A7  
 Poole T. S. et al., 2008, MNRAS, 383, 627  
 Poutanen J., Zdziarski A. A., Ibragimov A., 2008, MNRAS, 389, 1427  
 Rani B., Gupta A. C., Joshi U. C., Ganesh S., Wiita P. J., 2011a, MNRAS, 413, 2157  
 Rani B., Gupta A. C., Wiita P. J., 2011b, Journal of Astrophysics and Astronomy, 32, 217  
 Rani B. et al., 2013, A&A, 552, A11  
 Roming P. W. A. et al., 2005, Space Sci. Rev., 120, 95  
 Schlafly E. F., Finkbeiner D. P., 2011, ApJ, 737, 103  
 Sikora M., Begelman M. C., Rees M. J., 1994, ApJ, 421, 153  
 Spiridonova O. I., Vlasyuk V. V., Moskvitin A. S., Bychkova V. S., 2015, The Astronomer's Telegram, 7004, 1  
 Tagliaferri G. et al., 2003, A&A, 400, 477  
 Vaughan S., Edelson R., Warwick R. S., Uttley P., 2003, MNRAS, 345, 1271  
 Vercellone S. et al., 2011, ApJ, 736, L38  
 Wagner S. J. et al., 1996, AJ, 111, 2187

**Table 4.** The identified flares in the light curves of  $U$ ,  $UVW2$ ,  $\gamma$ -ray and X-ray bands, and the fit parameters of the flare profile (equation 7). The following columns present: (1) the studied energy band; (2) the time interval of a flare; (3) the flare symbol; (4) the approximate time of the peak (5) the rise time; (6) the decay time; (7) the calculated time of a peak; (8) the symmetry coefficient.

Energy band (1)	Time interval (2) (d)	Flare symbol (3)	$t_0$ (4) (MJD-57000)	$T_r$ (5) (d)	$T_d$ (6) (d)	$t_m$ (7) (MJD-57000)	$\xi$ (8)
<i>Swift</i> /UVOT( $U$ )	43.4-53.0	B	$48.15 \pm 0.66$	$2.47 \pm 0.82$	$1.15 \pm 0.58$	47.55	-0.37
<i>Swift</i> /UVOT( $U$ )	54.5-64.3	C	$55.64 \pm 0.66$	$1.03 \pm 0.25$	$5.22 \pm 2.69$	57.03	0.67
<i>Swift</i> /UVOT( $U$ )	64.0-70.2	D	$67.82 \pm 0.20$	$2.59 \pm 0.63$	$0.49 \pm 0.14$	67.14	-0.68
<i>Swift</i> /UVOT( $U$ )	70.7-75.2	E	$73.27 \pm 0.39$	$1.94 \pm 0.73$	$0.58 \pm 0.29$	72.73	-0.54
<i>Swift</i> /UVOT( $UVW2$ )	42.7-53.0	B	$47.84 \pm 0.70$	$2.34 \pm 0.64$	$1.09 \pm 0.46$	47.27	-0.36
<i>Swift</i> /UVOT( $UVW2$ )	53.0-64.3	C	$56.46 \pm 0.61$	$0.80 \pm 0.42$	$2.60 \pm 1.19$	57.18	0.53
<i>Swift</i> /UVOT( $UVW2$ )	64.0-70.7	D	$67.93 \pm 0.29$	$3.23 \pm 0.95$	$0.61 \pm 0.22$	67.08	-0.68
<i>Swift</i> /UVOT( $UVW2$ )	70.7-75.2	E	$73.41 \pm 0.41$	$2.21 \pm 0.86$	$0.60 \pm 0.33$	72.80	-0.57
<i>Swift</i> /XRT	53.4-62.6	C	$55.88 \pm 0.42$	$0.17 \pm 0.14$	$3.15 \pm 0.97$	56.34	0.90
<i>Swift</i> /XRT	62.6-71.7	D	$68.15 \pm 0.21$	$3.58 \pm 1.28$	$0.20 \pm 0.25$	67.60	-0.89
<i>Fermi</i> /LAT	31.5-42.5	A	$38.11 \pm 0.76$	$0.77 \pm 0.48$	$2.05 \pm 1.00$	38.66	0.45
<i>Fermi</i> /LAT	53.5-64.5	C	$55.50 \pm 0.35$	$0.39 \pm 0.30$	$1.94 \pm 1.01$	56.02	0.67

**Table 5.** The maxima of the CCF distribution. The following columns present: (1) the instruments used in the calculation; (2) the calculated value of the time lag; (3) the Pearson correlation coefficient for a given time lag, and (4) the likelihood of the given time lag.

Instruments (1)	$t_{lag}$ (d) (2)	$R$ (3)	Likelihood (4)
<i>Fermi</i> /LAT- <i>Swift</i> /UVOT( $V$ )	$1.31_{-0.29}^{+0.23}$	$0.88_{-0.06}^{+0.05}$	0.0331
<i>Fermi</i> /LAT- <i>Swift</i> /UVOT( $V$ )	$0.22_{-0.26}^{+0.24}$	$0.88_{-0.08}^{+0.06}$	0.0306
<i>Fermi</i> /LAT- <i>Swift</i> /UVOT( $B$ )	$-0.04_{-0.19}^{+0.19}$	$0.88_{-0.08}^{+0.06}$	0.0215
<i>Fermi</i> /LAT- <i>Swift</i> /UVOT( $U$ )	$-0.13_{-0.10}^{+0.15}$	$0.90_{-0.06}^{+0.05}$	0.0199
<i>Fermi</i> /LAT- <i>Swift</i> /UVOT( $U$ )	$0.92_{-0.13}^{+0.18}$	$0.91_{-0.06}^{+0.04}$	0.0244
<i>Fermi</i> /LAT- <i>Swift</i> /UVOT( $UVW1$ )	$1.06_{-0.29}^{+0.19}$	$0.84_{-0.08}^{+0.07}$	0.0184
<i>Fermi</i> /LAT- <i>Swift</i> /UVOT( $UVM2$ )	$0.22_{-0.08}^{+0.03}$	$0.90_{-0.07}^{+0.05}$	0.0517
<i>Fermi</i> /LAT- <i>Swift</i> /UVOT( $UVW2$ )	$0.47_{-0.26}^{+0.07}$	$0.85_{-0.07}^{+0.06}$	0.0712
<i>Fermi</i> /LAT- <i>Swift</i> /XRT	$10.76_{-0.29}^{+0.39}$	$0.59_{-0.13}^{+0.12}$	0.0129
<i>Fermi</i> /LAT- <i>Swift</i> /XRT	$17.99_{-0.19}^{+0.20}$	$0.57_{-0.16}^{+0.14}$	0.0114
<i>Fermi</i> /LAT- <i>Swift</i> /XRT	$20.52_{-0.06}^{+0.21}$	$0.57_{-0.22}^{+0.19}$	0.0151

White R. L., Becker R. H., 1992, ApJS, 79, 331

Wiercholska A., Siejkowski H., 2015, MNRAS, 452, L11

Wilks S. S., 1938, Ann. Math. Statist., 9, 60

Wright E. L. et al., 2010, AJ, 140, 1868